Ultrasonics Sonochemistry 93 (2023) 106305

Contents lists available at ScienceDirect

Ultrasonics Sonochemistry

journal homepage: www.elsevier.com/locate/ultson

Ultrasonic surface acoustic wave-assisted separation of microscale droplets with varying acoustic impedance

Mushtaq Ali, Jinsoo Park *

Department of Mechanical Engineering, Chonnam National University, Yongbong-ro 77, Buk-gu, Gwangju 61186, Republic of Korea

ARTICLE INFO

Keywords:
Ultrasonic surface acoustic wave
Acoustofluidics
Droplet separation
Acoustic radiation force
Acoustic impedance

ABSTRACT

In droplet-based microfluidic platforms, precise separation of microscale droplets of different chemical composition is increasingly necessary for high-throughput combinatorial chemistry in drug discovery and screening assays. A variety of droplet sorting methods have been proposed, in which droplets of the same kind are translocated. However, there has been relatively less effort in developing techniques to separate the uniform-sized droplets of different chemical composition. Most of the previous droplet sorting or separation techniques either rely on the droplet size for the separation marker or adopt on-demand application of a force field for the droplet sorting or separation. The existing droplet microfluidic separation techniques based on the in-droplet chemical composition are still in infancy because of the technical difficulties. In this study, we propose an acoustofluidic method to simultaneously separate microscale droplets of the same volume and dissimilar acoustic impedance using ultrasonic surface acoustic wave (SAW)-induced acoustic radiation force (ARF). For extensive investigation on the SAW-induced ARF acting on both cylindrical and spherical droplets, we first performed a set of the droplet sorting experiments under varying conditions of acoustic impedance of the dispersed phase fluid, droplet velocity, and wave amplitude. Moreover, for elucidation of the underlying physics, a new dimensionless number AR_D was introduced, which was defined as the ratio of the ARF to the drag force acting on the droplets. The experimental results were comparatively analyzed by using a ray acoustics approach and found to be in good agreement with the theoretical estimation. Based on the findings, we successfully demonstrated the simultaneous separation of uniform-sized droplets of the different acoustic impedance under continuous application of the acoustic field in a label-free and detection-free manner. Insomuch as on-chip, precise separation of multiple kinds of droplets is critical in many droplet microfluidic applications, the proposed acoustofluidic approach will provide new prospects for microscale droplet separation.

1. Introduction

A variety of microfluidic platforms have been established to facilitate microscale chemical and biomedical assays [1,2]. In particular, droplet-based microfluidic systems, where liquid spheres are dispersed into another immiscible liquid, are broadly used to provide independent environments for the encapsulated samples in numerous applications including drug screening [3,4], biological assays [5,6], and combinatorial chemistry [7]. Droplet-based microfluidics has experienced an unprecedented development in the last decade since the droplets, usually on the nano- to picolitre scale, can be produced and processed at high-throughput where the encapsulated samples within a droplet are isolated in the engineered microenvironment without cross-contamination, Taylor dispersion, or undesirable sample loss. Most droplet microfluidic applications involve unit operations, which serve basic building blocks of the droplet microfluidic applications, such as sorting, separation, splitting, merging, reinjection, and trapping.

Droplet separation with precise control of their trajectory within the microchannel are essential in various droplet microfluidic applications. Variety of active and passive techniques are available for separation of microdroplets. In inertial microfluidics platform, deterministic lateral displacement [8,9] and pinched flow fractionation [10] are most famous size-based droplet separation techniques. Recently, Chang *et al.* [11] demonstrated deformation-based droplet separation technique based on droplet viscosity, velocity, and volume. Li *et al.* [12] achieved inertial microfluidic droplet separation based on size. These passive methods provide simple operation at high-throughput; however, their practical applicability may be limited due to the inability of on-demand droplet

* Corresponding author.
E-mail address: jinsoopark@jnu.ac.kr (J. Park).

https://doi.org/10.1016/j.ultsonch.2023.106305
Received 2 October 2022; Received in revised form 15 January 2023; Accepted 17 January 2023
Available online 18 January 2023
1350-4177/© 2023 The Authors. Published by Elsevier B.V. This is an open access article under the CC BY-NC-ND license (http://creativecommons.org/licenses/by-nc-nd/4.0/).

manipulation, the formation of unwanted by-products, and heavy dependence on fluid properties, flow conditions and microchannel geometry. Alternatively, active approaches based on dielectrophoresis [13,14], Optophoresis [15,16], magnetophoresis [17,18], acoustophoresis [19,20], and thermocapillary [21,22] offer versatile droplet separation for practical applications.

The on-chip droplet separation process is associated with markers such as size [8], deformability [11], intrinsic properties [15] and additional labels [23]. However, available droplet separation devices based on their properties still demand several upgrades, such as the capability to separate multiple droplets simultaneously, the ability to separate high-speed droplets, and successful separation considering significant retention distance. Jung *et al.* [15] and Cho *et al.* [16] suggested the optofluidic separation of the droplets possessing different concentration of Calcium Chloride in an aqueous solution. They produced two kinds of droplets with different refractive index mismatch and investigated the droplet lateral displacement when the droplets were subject to an optical radiation force. Nevertheless, they only performed droplet sorting experiments of single kind and the droplet streamwise velocity allowed for successful separation were highly limited to < 10 mm/s under continuous laser excitation at ~ 5 W. Niu *et al.* [24] demonstrated separation of water and ethylene glycol droplets based on their dielectric constant; however, their method needs charged droplets for detection. In their work, Zhao *et al.* [14,25] used dielectrophoresis for separation of the hexafluorophosphate and silicone droplets based on electrical conductivity. Despite successful separation of two droplets of different chemical species, their dielectric device is only applicable for ionic or charged droplets for the separation operation and involve high electrical power (~650 V). Furthermore, fluorescence activated droplet sorting (FADS) methods have been developed for various droplet microfluidic applications including detecting enzyme activity [13,26]. However, these methods require both the presence of a fluorophore label within the droplets for detection and on-demand laser excitation, and they are not applicable to simultaneous separation of multiple droplets with varying chemical composition in a label-free and detection-free manner.

Herein, we propose an acoustofluidic method for on-chip, label-free, detection-free droplet separation based on chemical composition by using ultrasonic surface acoustic wave (SAW)-induced acoustic radiation force (ARF). By utilizing the ARF acting on the droplets of dissimilar chemical composition, which leads to different acoustic impedance values, we can translocate the microscale water-in-oil droplets into different outlets in a deterministic manner for high-throughput droplet separation. For in-depth investigation on the SAW-induced ARF acting on the droplets, we conducted ray acoustic analysis and introduced a new dimensionless AR_D, which was defined as the ratio of the ARF to the drag force acting on the droplets. The experimental results of droplet sorting of single kind under varying acoustic impedance contrast across the droplet interface, wave amplitude, and droplet velocity were found to be in good agreement with the theoretical estimation based on ray acoustics. Based on the findings, we achieved the acoustofluidic separation of the uniform-sized droplets of different chemical composition without any labelling on droplets or detection prior to separation for the first time. We believe that the proposed ultrasonic SAW-based acoustofluidic approach is a promising next-generation technique for on-chip droplet separation.

2. Materials and methods

2.1. Device configuration and operation

In this study, a cross-type acoustofluidic chip was used which is composed of polydimethylsiloxane (PDMS) microchannel affixed to a piezoelectric lithium niobate ($LiNbO_3$) substrate and slanted finger interdigital transducer (SFIT), as shown in Fig. 1(a). Similar cross-type acoustofluidic devices were previously used for particle separation [27,28]. The resonant frequency of the SFIT was estimated by dividing the speed of sound in $LiNbO_3$ (c_s) by the acoustic wavelength (λ), i.e., $f_{resonant} = c_s/\lambda$, and the actual working frequency range was measured to be 110–138 MHz. In our cross-type microfluidic chip, the PDMS microchannel was aligned in front of the SFIT such that the SAWs were allowed to propagate normal to the flow direction. An acoustic window was introduced in the microchannel to minimize the undesirable wave attenuation in the PDMS by viscoelastic damping [29]. The microchannel comprised of four inlets for two dispersed phase fluids (i and iii), a continuous phase fluid flows (ii) at a double T-junction, and one sheath fluid flow (iv), and two outlets (v and vi). For the droplet separation experiments, the aqueous liquids of two kinds and the continuous phase oil met at the double T-junction. Two kinds of droplets were alternatively produced when the continuous phase fluid encountered with the disperse phase fluids from both sides. A single kind of droplets were produced by utilizing only one dispersed phase fluid for the droplet sorting experiments. In the proposed system, a Hele-Shaw geometry was utilized having a small microchannel height compared to the channel width. The dimensions of the microchannel used for cylindrical droplets sorting and separation experiments were such that the width of the continuous phase channel (w_c) was 80 μm, the width of narrow constriction structure of the dispersed phase channel (w_d) was 40 μm, and the height (h) was 50 μm. A tapered microchannel geometry was used for the dispersed phase fluids to reduce the flow instability and prevent the undesirable droplet coalescence at the double T-junction [30]. The additional sheath flow was introduced to control interdistance between droplets and the droplet velocity (V_d) in the acoustic field. For the experiments of the spherical droplets, we utilized a microchannel with $w_c = w_d = 30$ μm and $h = 180$ μm. The main

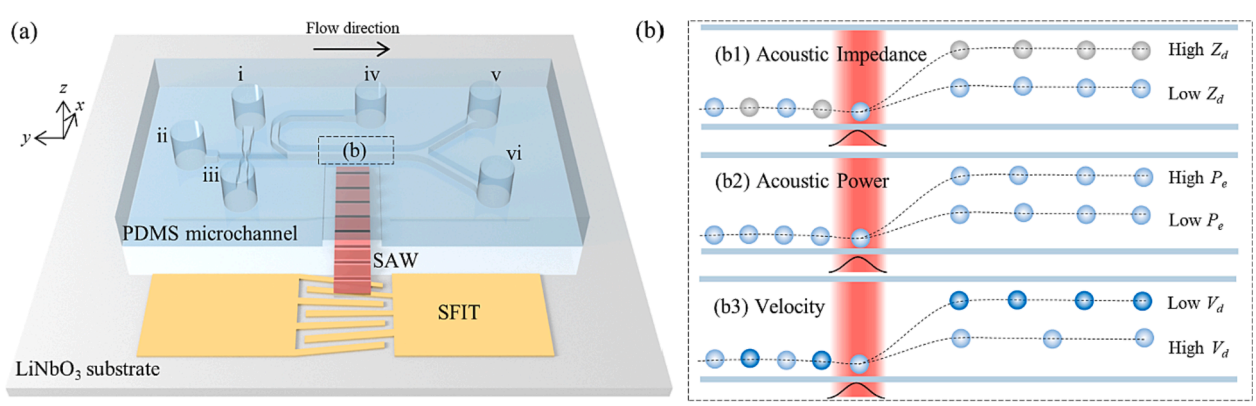

Fig. 1. (a) A schematic diagram of an acoustofluidic chip for separation of microscale droplets by surface acoustic wave (SAW)-induced acoustic radiation force (ARF). (b) Trajectories of droplets with varying (b1) acoustic impedance, (b2) acoustic power and (b3) droplet streamwise velocity, when they are exposed to acoustic field.

microchannel where the droplets interacted with the acoustic field has the width (w_a) of 500 μm and 600 μm for droplet sorting and separation experiments, respectively. OptiPrep™ (composed of 60 % iodixanol in water with a density of 1.320 g/ml, Sigma Aldrich) and deionized (DI) water at varying mixing ratio were used as the dispersed phase liquids to produce the droplets of varying acoustic impedance value. These liquids have acoustic impedance values of 2 MRayl (OptiPrep™) and 1.5 MRayl (DI water), respectively. OptiPrep™ is a widely used liquid in biomedical science, especially for clinical testing since it is non-ionic and non-toxic to cells [31,32]. A fluorocarbon oil (HFE-7500, 3 M; Z_c = 1.01 Mrayl; μ_c = 1.24 cP) was chosen as the continuous phase fluid as well as sheath fluid such that there was considerable acoustic impedance contrast between the droplets and the carrier fluid. A non-ionic, biocompatible surfactant (Pico-Surf™ 1) was added to the carrier fluid to stabilize droplet production and avoid undesirable coalescence of the droplets in oil.

2.2. Working mechanism

Rayleigh-type travelling SAWs are produced from an SFIT by the inverse piezoelectric effect when an AC signal with the resonant frequency of the SFIT is applied to the transducer. The acoustic beamwidth (w_0) of the Gaussian-profile SAWs produced by the SFIT was carefully designed as w_0 = 101.26 μm so that droplet diameter was comparable to the beamwidth for the droplets to experience the ARF effectively [33]. The standard interdigital transducer with parallel electrode fingers with the same effective acoustic beamwidth can be also used as an alternative [34]. The Rayleigh-type SAWs, propagating on the piezoelectric substrate, refracted into the fluid domain within the microchannel in the form of longitudinal waves (LWs) at the Rayleigh angle. The refracted waves can be decomposed into the horizontal component in the wave propagation direction and the vertical component in the direction perpendicular to the wave propagation, as well as the substrate. In the microchannels used in the experiments, the height was much smaller than the width. The cylindrical and spherical droplets were geometrically confined in the Hele-Shaw microchannel such that the droplet vertical motion was highly restricted. Despite the fact that the vertical contribution was neglected, the theoretical model based on the ray acoustics approach provided useful physical insights to investigate the phenomena observed in the experiments. When exposed to the SAW-induced acoustic field, the microscale water-in-oil droplets flowing in the microchannel experience the ARF due to the inhomogeneous geometrical wave scattering off the droplets [35], induced by a significant acoustic impedance contrast across the water/oil interface [36,37]. The ARF can be decomposed in the scattering component in the wave propagation direction and the gradient component in the directions perpendicular to the wave propagation [38]. The droplet sorting and separation operations were achieved by the droplet lateral migration in the wave propagation direction due to the scattering component of the ARF. The gradient component of the ARF acts in two directions (one in the flow direction and the other in the direction opposite to the flow, both of which are perpendicular to the wave propagation). The droplets with different acoustic impedance contrast values showed different droplet trajectories; consequently, the sorting and separation experiments were performed by changing acoustic impedance (Z_d) of the dispersed phase (Fig. 1(b1)), acoustic power (P_e) applied to the transducer (Fig. 1(b2)) and droplet streamwise velocity (Fig. 1(b3)). A higher acoustic impedance value results in an increase in the ARF magnitude, resulting in an increased retention distance for the droplet and vice versa. The acoustic impedance (Z) of any medium defines the resistance to the acoustic propagation in the medium such that $Z = \rho c$, where ρ and c are the density and speed of sound of that medium.

As in our earlier studies [36,37], a ray acoustics approach, in which acoustic waves are regarded as a set of momentum-carrying phonon rays in analogous to ray optics [38–40], was used to theoretically investigate the ARF acting on the droplets under varying conditions. As shown in Fig. 2(a), the Gaussian acoustic beam incident on liquid droplets is assumed to be a combination of rays with a finite momentum (p). Sequential wave reflection and transmission occur as the acoustic beam interacts with the droplet interface, and the ARF acting on the droplets can be obtained by determining the momentum change of a beam obeying Snell's law. In our theoretical model, the LWs were assumed to be coaxial and loosely focused, where w_o was significantly larger than the λ. The dynamic droplet migration in the acoustic field was simplified in our ray acoustics model, where the static droplet was exposed to a coaxial Gaussian-profile acoustic wave, for quantitative investigation on the ARF acting on the droplets. In both experiments and numerical calculation, we assumed the continuous application of the acoustic wave on the droplets. When the $D_d > h$, the droplets were assumed to be vertically squeezed between top and bottom walls, having a cylindrical shape. Below is the expression for the scattering component of acoustic radiation force, $F_{s,c}$, as described in our previous studies [36,37]:

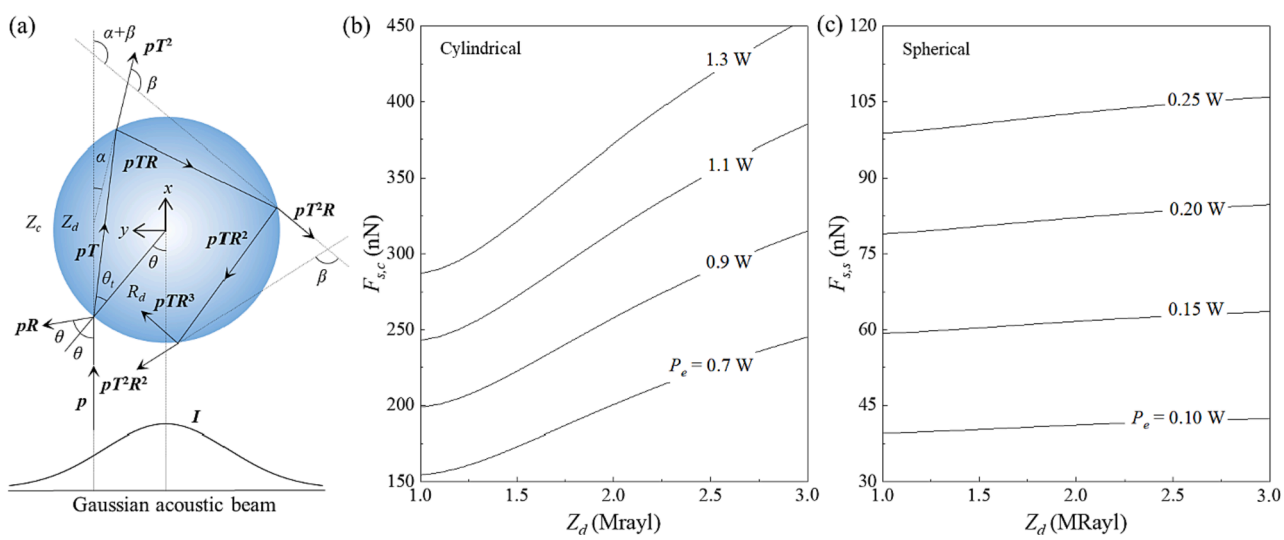

Fig. 2. (a) A schematic diagram of the phonon ray path in ray acoustics, when interacting with the medium of different acoustic impedance, is used to calculate acoustic radiation force. (b) Numerically calculated results using the ray acoustic approach for cylindrical Hele-Shaw droplets. The scattering component of acoustic radiation force acting on cylindrical droplets ($F_{s,c}$) was plotted as a function of acoustic impedance (Z_d) of the dispersed phase. (c) The scattering component of acoustic radiation force acting on spherical droplets ($F_{s,s}$) was plotted as a function of Z_d.

$$F_{s,c} = \frac{hD_d}{c_c}\int_0^{\pi/2} I(\theta)Q_x cos(\theta)d\theta \quad (1)$$

$$Q_x = 1 + Rcos(2\theta) - \frac{T^2\{cos(2\theta - 2\theta_t) + Rcos(2\theta)\}}{1 + R^2 + 2Rcos(\theta_t)} \quad (2)$$

where I is the acoustic intensity, c_c denotes the speed of sound in the continuous fluid, θ is the incident angle and θ_t is the transmission angle. The Fresnel reflection (R) and transmission (T) coefficients are defined as: [39]

$$R = \left|\frac{Z_d/cos(\theta_t) - Z_c/cos(\theta)}{Z_d/cos(\theta_t) + Z_c/cos(\theta)}\right|^2 \quad (3)$$

$$T = 1 - R \quad (4)$$

Fig. 2(b) shows the theoretical calculation of $F_{s,c}$ as a function of Z_d based on the ray acoustic model when $D_d = 105$ μm and $h = 50$ μm. The wave amplitude is proportional to the P_e applied to the SFIT. At a fixed P_e and the same continuous phase fluid, the ARF increases with increasing acoustic impedance value of the dispersed phase fluid as the wave reflection dominates over transmission. For the same dispersed and continuous phase fluids, the droplets experience increased SAW-induced ARF under increased P_e conditions. The ARF acting on the droplets in the geometric scattering regime originates from the serial wave reflection and transmission at the liquid–liquid interface. As the impedance mismatch increases, the reflected portion increases accordingly, resulting in an increase in the magnitude of the ARF. Due to the curved interface of the droplets exposed to the acoustic wave, the reflection coefficient is not zero even when the acoustic impedance values of the dispersed and continuous phase liquids are the same due to the rays having non-zero incident angles. Moreover, the acoustically transparent liquid–liquid interface, in which the acoustic impedance of the two liquids are the same, deforms when exposed to an acoustic beam, as reported by Issenmann *et al.* [41]. This interface deformation occurs toward the less compressible liquid, which was the dispersed phase liquid of the droplet in our experiments. The deformed interface resulted in the varying radius of curvature along the droplet interface, causing the pressure imbalance within the droplets. As a consequence, the droplets are assumed to migrate in the wave propagation direction due to the in-droplet pressure gradient. Between the two walls of the Hele-Shaw microchannel, the generated cylindrical droplets were vertically squeezed. It dramatically increases the drag force, which can be estimated as $F_{d,c} = 6\pi\mu_c D_d^2 V_d/h$ where μ_c is the dynamic viscosity continuous phase fluid [29].

On the other hand, in case of $D_d < h$, the droplets are supposed to be spherical. The scattering component of acoustic radiation force on the sphere, $F_{s,s}$, is given as:

$$F_{s,s} = \frac{1}{4c_c}\int_0^{2\pi}\int_0^{\pi/2} I(D_d,\theta,\varphi)Q_x {D_d}^2 sin(2\theta)d\theta d\varphi \quad (5)$$

where φ is the polar angle. Fig. 2(c) shows the numerically calculated results for the scattering component of the ARF acting on the spherical droplets (when $D_d = 105$ μm) as a function of Z_d at varying electrical input power applied to the transducer. Unlike the numerical calculated results of cylindrical droplet, we can see the small variation in the magnitude of F_s even when the acoustic impedance values of a dispersed phase. Possible reason of the contrast between Fig. 2(b) and Fig. 2(b) could be justified from the governing equations. As the ARF acting on the cylindrical component is proportional to the height of microchannel as well as diameter of the droplet (Eq. (1)). On the other hand, ARF on spherical droplets are proportional to the square of droplet diameter (Eq. (5)). The Stoke's drag force for a spherical droplet dispersed in a carrier fluid and within a confined microchannel is given as $F_{d,s} = 3\pi\mu^* D_d V_d$ where where μ^* is the effective viscosity which incorporates the viscosities of both continuous and dispersed phases and can be expressed as:

$$\mu^* = \mu_c\frac{1 + 2\mu_c/3\mu_d}{1 + \mu_c/\mu_d} \quad (6)$$

where μ_d is the dynamic viscosity of a dispersed phase fluid. As in the results for cylindrical droplets, the spherical droplets are subject to a greater ARF as the acoustic impedance of the droplet dispersed phase fluid increases under the same continuous oil phase fluid at fixed P_e. At the same fluid conditions, the droplets experience an increased SAW-induced ARF as the applied electrical power to the SFIT increases.

3. Results and discussion

3.1. Sorting and separation of Hele-Shaw droplets

Fig. 3 (a) shows the staked microscopy images of the droplet sorting experiments with varying acoustic impedance ratio (Z_d/Z_c) ranging from 1.49 to 1.98. For Z_d–based droplet sorting experiments, we used the mixed solution of DI water and OptiPrep™ as a dispersed phase fluid such that their acoustic impedance ratio ranges between 1.49 (pure DI water) and 1.98 (OptiPrep™). The acoustic impedance for the mixed solution at varying ratio was calculated as 1.58, 1.68, 1.78 and 1.88 with minimal or no changes in viscosity [42]. Using a single T-junction upstream, we produced equal-sized aqueous droplets ($D_d \cong 105$ μm) whose acoustic impedance varied depending on the ratio of the DI water and iodixanol under the fixed droplet velocity ($V_d \cong 10.8$ mm/s). Since the droplets in the Hele-Shaw microchannel experience a considerable drag force dependent on droplet diameter and velocity, we kept V_d and D_d fixed in the Z_d–based sorting and separation experiments to isolate the Z_d effect under uniform flow-induced drag force. Fig. 3(a) shows different droplet trajectories at $Z_d/Z_c = 1.49$–1.98 under the fixed $P_e = 0.5$ W. Unless otherwise specified, we utilized the 120 MHz SAW applications to observe the impact of ARF on the droplet. As the Z_d/Z_c value increased from 1.49, 1.58, 1.68, 1.78, 1.88 to 1.98, the droplet retention distance d_R was measured to increase from 111.72, 120.81, 142.82, 148.01, 167 to 186.37 μm, respectively. This can be attributed to the increased portion of the wave reflection at the droplet interface compared to the wave transmission, resulting in an increase in the SAW-induced ARF magnitude. Vindicating the theoretical prediction discussed in previous section, we observed a linear relationship between acoustic power and retention distance for increasing acoustic impedance ratios. Fig. 3(b) shows the various trajectories of the water droplets ($Z_d/Z_c = 1.49$) when they were exposed to SAW-induced ARF in the main acoustic assessment zone by altering the applied electrical power between 0.3 and 1.3 W. Without applying the acoustic field, the droplet travels to the outlet hydrodynamically without showing any deflection. With increasing acoustic power, droplets deflected in the main acoustic deflection region, and the retention distance d_R were measured until the maximum point, taking the onset of acoustic radiation force as an origin. As the P_e value increased from 0.3, 0.5, 0.7, 0.9, 1.1 to 1.3 W, the droplet d_R was measured to increase from 84.92, 111.71, 146.72, 169.43, 203.64 to 243.91 μm, respectively. This is due to the fact that the ARF driven by LWs is proportional to the applied acoustic power [43]. When the transducer efficacy is amplified by simply tuning the P_e, the incident ray hitting the droplet interface changes the magnitude of reflected and transmitted rays.

In addition to ARF magnitude, the measured retention distance is also dependent on the drag force of the droplet moving in the microchannel. As discussed in previous section, drag force on cylindrical droplets are proportional to the droplet diameter, droplet speed, and height of the microchannel. When h and D_d kept constant, a droplet having greater speed would be subjected to a localized acoustic force for a shorter amount of time, resulting in a smaller retention distance. On the other hand, slower droplet remains longer in the acoustic assessment zone, causing a larger retention distance. Hence the performance of the

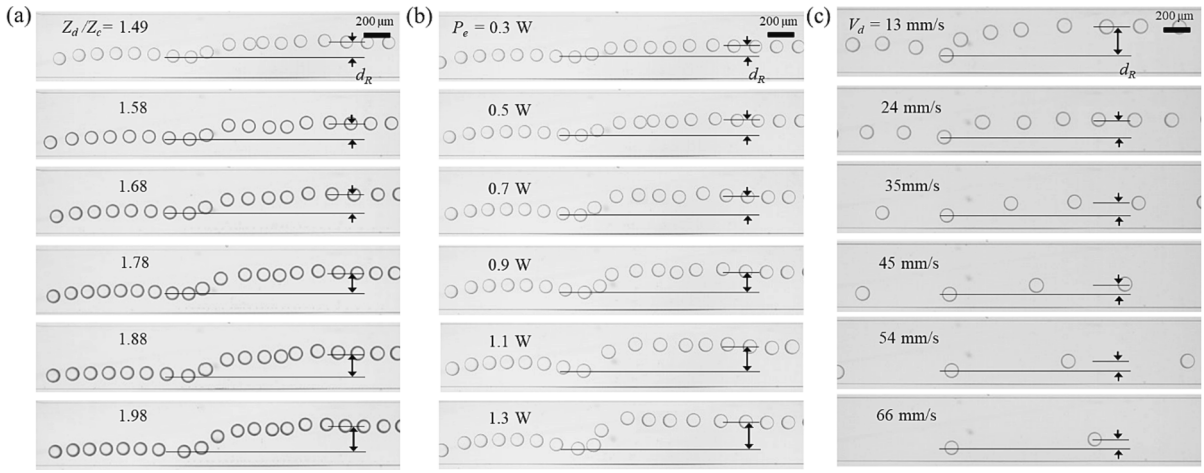

Fig. 3. Experimental stacked microscopy images of cylindrical droplet sorting at $f = 120$ MHz. (a) Sorting based on acoustic impedance (Z_d/Z_c of 1.49–1.98) with varying retention distance at $P_e = 0.5$ W. The deflection of droplets having a larger Z_d value is greater than that of droplets having a smaller Z_d. (b) Sortingof DI water droplet ($Z_d/Z_c = 1.49$) with varying P_e (0.3–1.3 W). (c) Sorting of DI water droplet ($Z_d/Z_c = 1.49$) varying droplet streamwise velocity from 13 to 66 mm/s at $P_e = 1.01$ W.

proposed approach is strongly reliant on the droplet streamwise velocity. Therefore, droplet behavior was further analyzed to achieve the V_d–based sorting experiments, and the flow rate of sheath fluid was carefully tuned from 50 to 10,000 µL/h. Fig. 3(c) shows the microscopic image of the V_d–based sorting of cylindrical droplets for varying droplet streamwise velocity from 13 to 66 mm/s at $P_e = 1.01$ W. As the V_d value increased from 13, 24, 35, 45, 54 to 66 mm/s, the droplet retention distance d_R was measured to decrease from 139.85, 105.44, 93.88, 77.25, 66.66 to 63.15 µm, respectively. This can be accredited to the increased magnitude of drag force, since the droplet moving faster will come into contact with more fluid particles in surrounding. This behavior could also be quantitatively discussed by using Eq. (7), which specifies that, AR_D number is inversely proportional to V_d.

For a better insight into the underlying phenomena and to predict the droplet behaviors, a dimensionless number, AR_D, has been introduced, which is defined as:

$$AR_D = \frac{(Z_d/Z_c)(P_e/\pi c_c)\left(D_d{}^2/w_o^2\right)}{\pi\left(\mu_c^2/\mu_d\right)D_d V_d} \tag{7}$$

The numerator in Eq. (7) represents the applied momentum per second and thus depicting the acoustic radiation force acting on a droplet while the denominator refers to the droplet drag force. Hence, AR_D number accounts for the combined effect of acoustic radiation force as well as the drag force. Additionally, the viscosity ratio of the continuous and dispersed phase fluids is also included to consider the effective viscosity that plays a role in the drag force acting on the droplets [15,44].

The dimensionless number AR_D is linearly proportional to the acoustic impedance contrast (Z_d/Z_c) and the applied electrical power (P_e) but inversely proportional to the droplet streamwise velocity (V_d) according to the definition. The observed d_R values were then scaled by the D_d to investigate the phenomena based on the normalized droplet retention distance with respect to the droplet size. Fig. 4 shows the influence of AR_D on the dimensionless droplet retention distance (d_R/D_d) with varying Z_d, P_e and V_d where the black solid line indicates $d_R/D_d = 4 \times 10^{-5}\ AR_D$. The least-square method was used to fit the experimental data for the linear relationship between AR_D and d_R/D_d. The dimensionless droplet retention distance (d_R/D_d) was found to be proportional to the AR_D number for varying Z_d, P_e as well as V_d. The ARF scattering component agreed well with the experimental results obtained by measuring retention distances for each droplet. The upright error bars representing the data points imply the standard deviation of the droplet retention distance.

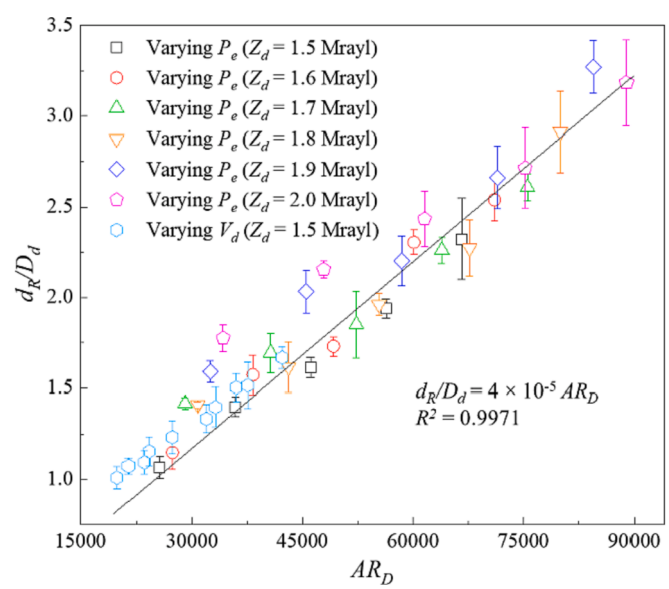

Fig. 4. Experimental results of the Z_d-based sorting of cylindrical droplets. Non-dimensionlized retention distances (d_R/D_d) is plotted as a function of dimensionless AR_D number.

Based on the investigation of sorting experiments of single kind we separated two droplets of same size but different acoustic impedance simultaneously and demonstrated Z_d–based separation of cylindrical droplets. When the acoustic impedance of the dispersed phase was changed, a linear trend in droplet retention distance was realized which is demonstrated in a droplet sorting experiment. This is because a droplet with a greater acoustic impedance experiences higher magnitudes of SAW-induced ARF than a droplet with a lower acoustic impedance as discussed in previous section. In this experiment, two droplets (droplet A and droplet B) were produced and separated, whose acoustic impedance values are $Z_{d,A} = 2.0$ MRayl and $Z_{d,B} = 1.5$ MRayl, as shown in Fig. 5(a). Without the application of acoustic force, both droplets travel hydrodynamically to one outlet (Fig. 5(a1)). When they experienced ARF by applying $P_e = 1.52$ W as shown in Fig. 5(a2), droplet A was literally pushed more along the axial direction of ARF than droplet B; consequently, their retention distances were 300 and 183 µm, respectively (see Supplementary Movie 1). The retention distance

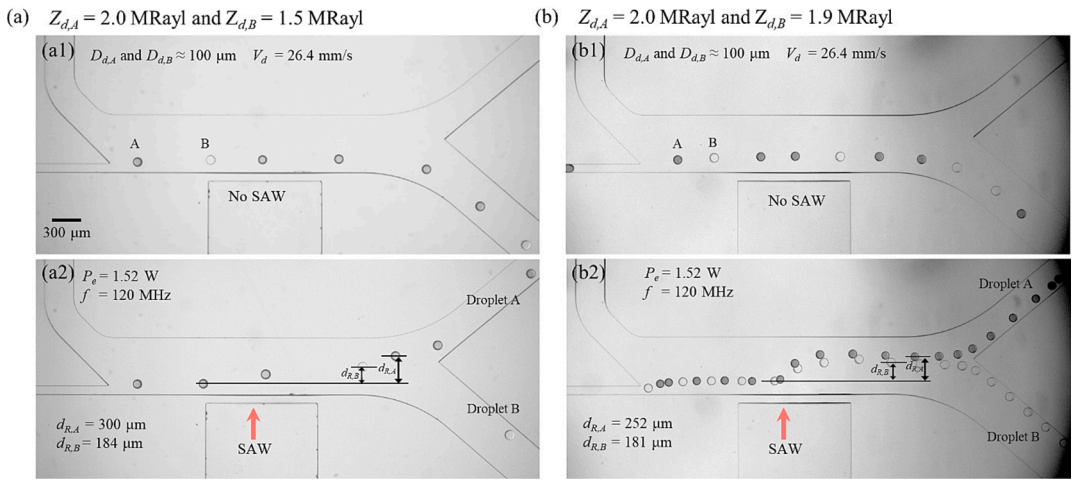

Fig. 5. Microscopy images of Z_d–based separation of cylindrical droplets having D_d = 100 μm, V_d = 26 mm/s, P_e = 1.52 W and f = 120 MHz. (a) Representation of simultaneous separation of two droplets ($Z_{d,A}$ = 2.0 MRayl and $Z_{d,B}$ = 1.5 MRayl). (a1) Without an acoustic field, two kinds of droplets moved toward the same outlet with their trajectories remained undeflected. (a2) Under the SAW-induced acoustic field two droplets were separated witnessing significant the Δ d_R. (b) Simultaneous separation of two droplets ($Z_{d,A}$ = 1.6 MRayl and $Z_{d,B}$ = 1.5 MRayl) having minimum Δ Z_d. (b1) Without an acoustic field, both droplets moved toward the same outlet undeflected. (b2) Under the SAW-induced acoustic field two droplets were separated witnessing a significant Δ d_R.

difference between two droplets (121 μm) because of acoustic impedance difference was significant to separate droplets into different outlets. The expanded width of main acoustic assessment zone was used for separation experiment in order to expose them to ARF for a to increase the retention distance difference (Δd_R). Furthermore, as shown in Fig. 3 (a), the droplet retention distance monotonically increases with increasing the acoustic impedance contrast. Based on the findings, two kinds of droplets are expected be separated even with a small acoustic impedance difference. However, the stability of the droplet separation can be ensured with a sufficient Δd_R, which also requires a sufficient ΔZ_d. In this regard, we demonstrated the acoustofluidic droplet separation droplets of with ΔZ_d = 0.5 Mrayl. We performed additional droplet separation experiments with ΔZ_d = 0.1 MRayl as shown in Fig. 5 (b), to verify that the droplets can be separated using the proposed method only with a small acoustic impedance difference. The simultaneous separation of these droplets was successful witnessing Δd_R of 71 μm despite having a minimum ΔZ_d (see also Supplementary Movie 1). In our sorting and separation experiments, we produced nanolitre droplets with a large surface area ($D_d \cong$ 100 μm) that predominately provides opportunities for the biological assays that cannot be encapsulated within a small volume [45,46].

The cylindrical and spherical droplets investigated in this study were in the geometrical scattering regime, where the droplet diameter (D_d) was much larger than the wavelength λ [35]. In the previous studies using longer-wavelength standing waves for droplet sorting [19,20], the D_d was comparable or much smaller than the λ in the fluid. For example, Li *et al.* [19] utilized the standing SAWs-induced ARF with their wavelength ranging from 360 to 400 μm only for the cylindrical droplets sorting with their diameter of 40–50 μm, without the droplet separation of multiple kinds. Also, in these studies, the droplets were assumed to as solid microspheres in the Mie scattering regime, and the droplet lateral migration (i.e., retention distance, d_R) was limited by the formation of the acoustic pressure nodes and antinodes [47]. Furthermore, when the droplet size diameter is comparable to the acoustic wavelength, the contribution of the travelling SAW-induced Eckart streaming effect would become significant, as reported by Schmid *et al.* [48] ($D_d \cong$ 25 μm; λ = 23–24.5 μm). Hence, we have chosen the parameters such as D_d, V_d, and P_e to maximize the difference in the Δd_R between the droplets of varying Z_d in the acoustofluidic device used in this study and to minimize the effects of the acoustic radiation effect to facilitate the separation of the equal-size droplets using the travelling SAW-induced ARF in a label-free, detection-free manner. We hypothesize that if the smaller droplets are used, the microchannel should be further optimized accordingly for droplet separation even with reduced Δd_R.

3.2. Sorting and separation of spherical droplets

Hypothesizing that excessive drag force could be avoided by utilizing smaller droplets in a broader microchannel, we produced multiple droplets such that diameter of the droplets was smaller than the height to achieve Z_d–based sorting and separation experiments. The sorting experiments for six types of droplets possessing different acoustic impedances ratios (1.49 to 1.98) were characterized exactly in a similar manner as Hele-Shaw droplets. Droplet diameter in these experiments was ~ 105 μm, however, unlike cylindrical droplets, we investigated spherical droplet at a much slower speed ($V_d \cong$ 4.5 mm/s) so that they can be exposed to ARF for a significant amount of time. Fig. 6(a) shows the experimental staked microscopy images of Z_d–based sorting of spherical droplets at P_e = 0.16 W. The d_R values of droplets having Z_d/Z_c of 1.49, 1.58, 1.68, 1.78, 1.88, and 1.98 are 282.8, 289.44, 302.03, 299.18, 208.47 and 320.3 μm, respectively. The retention distance for all the results are linearly increasing for increasing acoustic impedance values validating the hypothesis based on ray-acoustics. In addition, much smaller magnitude of force was needed for spherical droplets to deflect from their original path significantly since we have avoided the drag force utilizing microchannel of higher height. Hence, the sorting experiments were characterized at much lower acoustic power i.e. in between 0.02 and 0.16 W as shown in Fig. 6(b). The alteration of these acoustic power causes the acoustic radiation force of different magnitude. As the P_e value increased from 0.02, 0.04, 0.06, 0.08, 0.10 to 0.12 W, the droplet retention distance d_R was measured to increase from 50.37, 100.88, 141.57, 170.41, 204.31 to 236.29 μm, respectively. When amplitude of acoustic power was increased to maximum voltage, the magnitude of ARF was increased and the droplets were translocated toward the maximum point resulting in highest d_R in main acoustic assessment zone. We were able to handle droplets at quite low acoustic power (<1.5 W for cylindrical droplets and < 0.6 W for spherical droplets) compared to other platforms, such as dielectrophoresis (4–1.8 kV_{p-p} [13], 0.6 kV_{p-p} [26]) and optophoresis (<5 W [15,16]).

We further extended our work on V_d–based sorting activity for spherical droplets and measured retention distances with an increasing flow rate of sheath fluid from 500 to 3500 μL/h keeping the other parameters fixed such that $D_d \cong$ 105 μm, P_e = 0.11 W, and f = 120 MHz. Fig. 6(c) shows the experimental microscopy images of DI water droplets

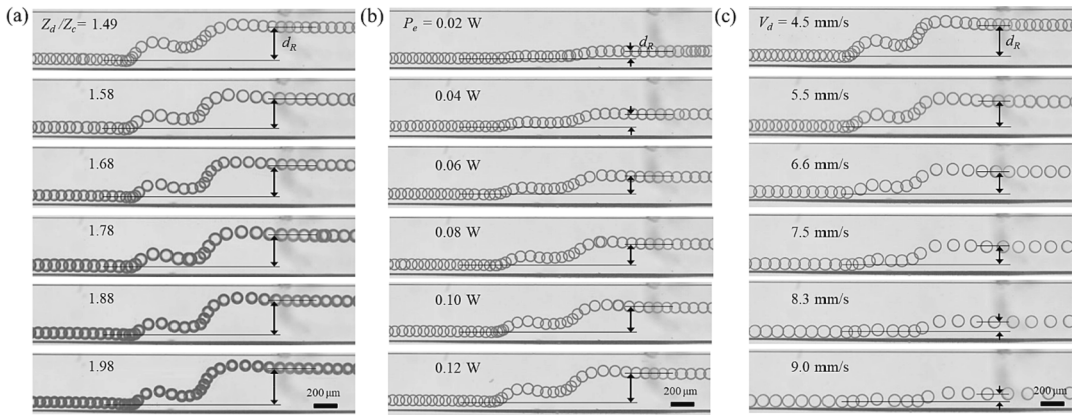

Fig. 6. Experimental stacked microscopy images of spherical roplet sorting at $f = 120$ MHz. (a) Sorting based on acoustic impedance (Z_d/Z_c of 1.49–1.98) with varying retention distance at $P_e = 0.16$ W. The deflection of droplets having a larger Z_d value is greater than that of droplets having a smaller Z_d, (b) Sortingof DI water droplet ($Z_d/Z_c = 1.49$) with varying P_e (0.02–0.12 W). (c) Sorting of DI water droplet ($Z_d/Z_c = 1.49$) varying droplet streamwise velocity from 4.5 to 9 mm/s at $P_e = 0.2$ W.

of different speed when the acoustic power was fixed at 0.2 W. The streamwise droplet velocity is proportional to flow-induced drag force, so at fixed acoustic radiation force, we altered droplet speed from 4.5 mm/s to 9 mm/s, and corresponding retention distances were measured. As the V_d value increased from 4.5, 5.5, 6.6, 7.5, 8.3, to 9 mm/s, the droplet retention distance d_R was measured to decrease from 273.26, 220.79, 170, 140.01, 130, to 98 μm, respectively. Finally, the plot between dimensionless retention distance and AR_D was performed for the overall results with varying Z_d, P_e and V_d as shown in Fig. 7. Once again, the dimensionless AR_D was found to be nearly proportional to the dimensionless retention distance (d_R/D_d). The dimensionless retention distance and AR_D were found to have a linear relationship as the fitted line using the least-square method indicates. However, compared to the Hele-Shaw droplets, the retention distance differences of spherical sorting experiments were not significant enough, since spherical droplets moving in the microchannel having a diameter much smaller than the height, thereby experiencing much smaller magnitude of drag force. This is witnessed in drag force equation presented in earlier section, which indicates that drag force experienced by cylindrical droplet is inversely proportional to the height of the microchannel. On the other hand, drag force on the spherical droplets are dependent on the diameter and the speed of the droplet. In addition, droplets may have experience wall-induced drag force of inconsistent magnitude depending on their spatial position in the main acoustic assessment zone as modeled by Jung *et al.* [15]. Lastly, cylindrical droplets being constrained between the top and bottom walls, vertical migration are limited compared to spherical droplets where they have enough space to move vertically. In the mid- and long-term, we intend to conduct a complete examination of the wall-induced drag force and vertical migration of the droplet within microchannel.

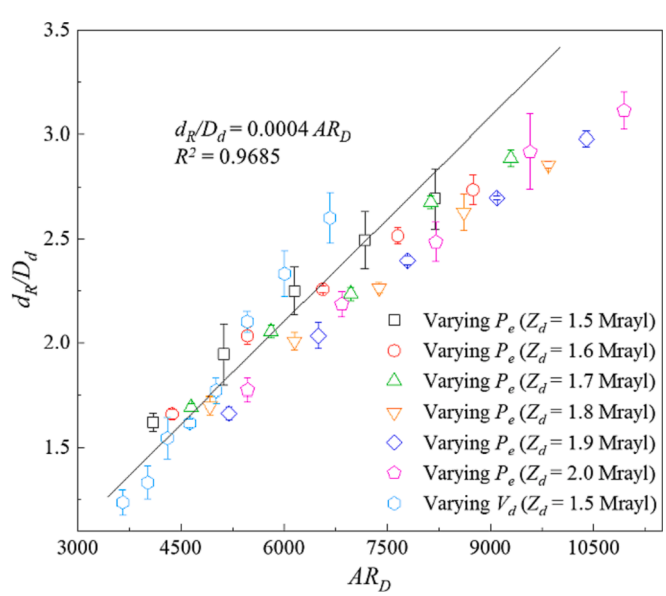

Fig. 7. Experimental result of the Z_d-based sorting of spherical droplets. Non-dimensionlized retention distances (d_R/D_d) is plotted as a function of dimensionless AR_D number.

It was noted from droplet sorting experiments of single kinds that retention distances difference of each experiments possessing different Z_d values was not significant as compared to cylindrical droplets. Similar behavior was also realized in Z_d–based separation results of spherical droplets and noted retention differences of two droplets was only 43 μm. Nevertheless, this difference between two droplets was significant to separate droplets into different outlets and successfully achieved Z_d–based separation results of spherical droplets. As shown in Fig. 8(a), two droplets (droplet A and droplet B) were produced and separated, whose acoustic impedance values are $Z_{d,A} = 2.0$ MRayl and $Z_{d,B} = 1.5$ MRayl. Without SAW, both droplets travel hydrodynamically to one outlet (Fig. 8(a1)). When they experienced ARF by applying $P_e = 0.15$ W as shown in Fig. 8(a2), droplet A was literally pushed more along the axial direction of ARF than droplet B; consequently, their retention distances were 226 and 206 μm, respectively (see Supplementary Movie 2). Furthermore, as shown in (Fig. 8(b)), an additional droplet separation experiments were performed with $Z_d = 1.5$ and 1.6 MRayl and verified that the droplets can be separated using the proposed method only with ΔZ_d of only 0.1 Mrayl (see also Supplementary Movie 2). As can be found in the movies, the upstream droplets decelerated right before the acoustic field due to the presence of the gradient component in the direction opposite to the flow and were laterally deflected by the scattering component of the ARF. Right after passing through the acoustic field, the downstream droplets accelerated due to the gradient component in the flow direction. With increasing P_e, the increased wave amplitude would amplify the contributions of both scattering and gradient components of the ARF.

It should be noted also that the droplet separation was achieved even at extraordinary speed (99 mm/s) with significant d_R which outperforms many existing droplet sorting devices offered by dielectrophoresis (2–3 mm/s [49] & 35 mm/s [23]) optophoresis (<15 mm/s [15,16]), and magnetophoresis (3.2 mm/s [50]). Furthermore, the droplet production rate was approximately 50 droplets per second; nonetheless, it was not the limited value in the proposed method. If the droplets were produced a priori at faster rates and injected into the microchannel, the number of

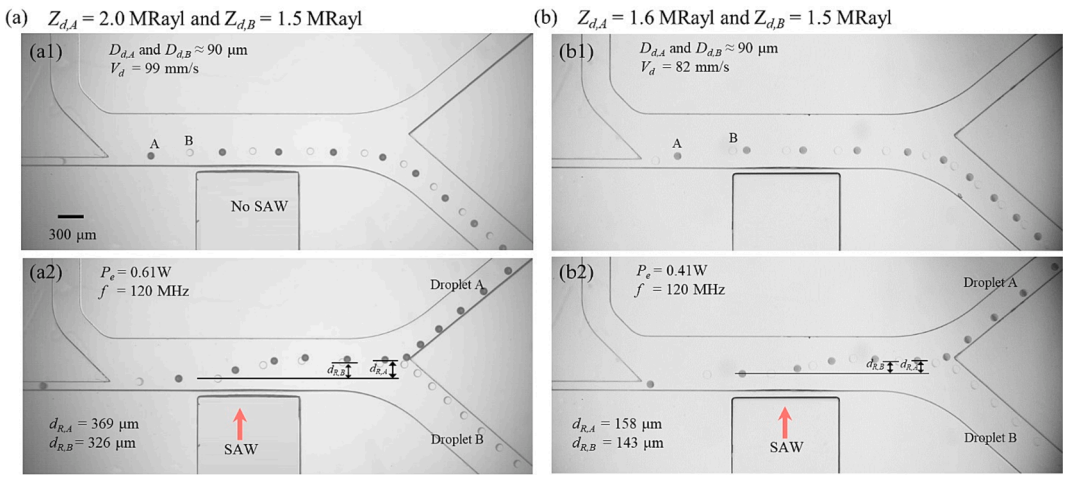

Fig. 8. Microscopy images of Z_d–based separation of spherical droplets having $D_d = 90$ μm, and $f = 120$ MHz. (a) Representation of simultaneous separation of two droplets ($Z_{d,A} = 2.0$ MRayl and $Z_{d,B} = 1.5$ MRayl) at $P_e = 0.61$ W and $V_d = 99$ mm/s. (a1) Without an acoustic field, two kinds of droplets moved toward the same outlet with their trajectories remained undeflected. (a2) With application of acoustic fled two droplets were separated witnessing significant the Δd_R. (b) Simultaneous separation of two droplets ($Z_{d,A} = 1.6$ MRayl and $Z_{d,B} = 1.5$ MRayl) having minimum ΔZ_d at and $P_e = 0.41$ W and $V_d = 82$ mm/s (b1) Without an acoustic field, both droplets moved toward the same outlet undeflected. (b2) With application of acoustic fled two droplets were separated witnessing a significant $\Delta\ d_R$.

the droplets separated per second would have been increased accordingly. Moreover, as can be predicted from our theoretical model with AR_D and validated by the experimental results, for improved throughput in droplet separation, the acoustic impedance contrast should be increased, the P_e should be increased, and the V_d should be decreased. However, it should be noted that the increased electrical power may induce the non-linear acoustic streaming body force acting on the droplets, which is not desirable for the separation of the equal-sized droplets by acoustic radiation. Droplet sorting and separation experiments in this study were performed under the P_e of < 1.5 W, which corresponds to 24.49 Vpp, much less than other microfluidic droplet sorting and separation techniques as explained in the earlier section. Despite the moderate electrical power level, there may have been the undesirable heating effect, which can result in thermo-capillary droplet migration. The thermo-capillary droplet migration velocity is inversely proportional to the viscosity of the dispersed phase fluid [22]. The viscosity slightly increases with increasing concentration of iodixanol in water [42]. In our experiments of the droplet sorting and separation, we observed that the d_R increased with increasing Z_d, which also involved increasing viscosity of the dispersed phase, leading to the decreased thermo-capillary droplet migration effect. Therefore, we can conclude that the primary working mechanism of the droplet sorting and separation proposed in this study is the surface acoustic wave-driven ARF, which causes the difference in the retention distance between multiple kinds of the droplets with varying acoustic impedance. In addition, we achieved the droplet sorting and separation operations in a wide range of the droplet velocity. The droplet velocity ranged from 13 to 66 mm/s for cylindrical droplets and from 4.5 to 99 mm/s for spherical droplets. The Peclet number for heat transfer is expressed as $\mathrm{Pe} = hV_d/D_t$ where D_t is the thermal diffusivity of the continuous phase fluid. The Pe value ranged from 18.07 to 91.77 and 22.52 to 495.58 for cylindrical and spherical droplets, respectively. Since the Pe was much greater than 1 in all experimental conditions, the heat diffusion required a much longer time compared to the convection. Therefore, we assumed that the moving droplets were not significantly affected by the heated side wall. Based on the ray acoustics model, the smaller droplets would experience the acoustic radiation force with decreased magnitude, and the difference in the droplet lateral migration would decrease accordingly, which suggests that the further optimized microchannel design is required for successful droplet separation at downstream bifurcation. As for the cylindrical droplets, we investigated the sorting and separation of the spherical droplets, whose size was much larger than the acoustic wavelength, in the geometrical scattering regime. Previously, Leibacher *et al.* [20] utilized the bulk acoustic wave-driven standing pressure nodes ($\lambda \cong 1000$ μm) for the acoustic sorting of the spherical droplets with the diameter of approximately 200 μm, not separation of multiple droplets as demonstrated in this work. In this long-wavelength approach, the droplet lateral migration was constricted by the locations of the acoustic pressure nodes and antinodes [47].

4. Experimental

The SFIT composed of Cr (30 nm) and Au (100 nm) was patterned on a 500 μm thick, 128° Y-cut, X-propagating $LiNbO_3$ substrate (MTI Korea) by e-beam evaporation and lift-off processes. A rectangular microchannel was made by soft lithography process by mixing PDMS base and curing agent (Sylgard 184A and 184B, Dow Corning) of ratio 10:1 (w/w). It is then bonded on the substrate via oxygen plasma bonding (Covance, Femto Science). Before conducting experiments, the bonded microchannel was coated with fluorocarbon liquid (EGC-1720, 3 M). The wet microchannel was then left in an oven at 85 °C for 30 min after the fluorocarbon liquid gently flowed through the channel. The SIFT was composed of total 40 electrode pairs, and the total aperture was 1000 μm. The frequency range of SFIT was between 110 and 138 MHz, with electrodes spacing ($\lambda/4$) varied from 7 to 9 μm, measured by a vector network analyzer (E5071B, Agilent Technologies), and SAW pulses were generated using Belektronig SAW generator (DE/BSG-F10, Belektronig).

Varied iodixanol concentration in water and deionized water (dispersed phase-1, Sigma Aldrich and dispersed phase-2, Sigma Aldrich) and fluorocarbon oil (continuous and sheath flow fluid, Novec™ 7500, 3 M) were flowed using syringe pumps (neMESYS Cetoni GmbH and Chemyx Fusion 4000). The Iodixanol droplets were dyed with Erioglaucine disodium salt (Sigma Aldrich) to differentiate amongst water droplets in separation experiments. To stabilize and avoid coalescence of the droplets in oil, 1 wt% Pico-Surf™ 1 biocompatible surfactant was added to the carrier fluid. Experimental results were recorded using a high-speed camera (VEO 710L, Phantom Ametek) mounted on a light microscope (IX73, Olympus) at 700 frames per second. Furthermore, mathematical modeling of acoustic radiation force and experimental results was analyzed using MATLAB and ImageJ software.

5. Conclusions

We developed an ultrasonic SAW-based acoustofluidic method for simultaneous separation of droplets with different acoustic impedance in a label-free, detection-free manner at high-throughput. The underlying physical mechanism was investigated by using ray acoustics analysis on the droplet sorting experimental data under varying working conditions of the acoustic impedance of dispersed phase fluid, acoustic power, and droplet streamwise velocity. For better understanding of the acoustofluidic droplet sorting and separation phenomena, a new dimensionless number AR_D, defined as a ratio of acoustic force based on ray acoustics and drag force, was introduced to find the relationship between the AR_D and the droplet lateral migration normalized by the droplet diameter. The proposed acoustofluidic technique can be utilized in many droplet microfluidic applications where label-free, detection-free and continuous separation of droplets with varying chemical composition is required.

Data availability

Data will be made available on request.

CRediT authorship contribution statement

Mushtaq Ali: Validation, Formal analysis, Investigation, Writing – original draft, Writing – review & editing. **Jinsoo Park:** Conceptualization, Methodology, Validation, Formal analysis, Writing – original draft, Writing – review & editing, Supervision, Funding acquisition.

Declaration of Competing Interest

The authors declare the following financial interests/personal relationships which may be considered as potential competing interests: Jinsoo Park reports financial support was provided by by National Research Foundation of Korea. Jinsoo Park reports equipment, drugs, or supplies was provided by Energy Convergence Core Facility in Chonnam National University.

Acknowledgments

This work was supported by the National Research Foundation of Korea (NRF) grants funded by the Korea government (MSIT) (Nos. 2020R1F1A1048611 and 2020R1A5A8018367). The microfluidic devices were fabricated by using a mask aligner (MDA-400S, MIDAS) at Energy Convergence Core Facility in Chonnam National University.

Appendix A. Supplementary data

Supplementary data to this article can be found online at https://doi.org/10.1016/j.ultsonch.2023.106305.

References

[1] G.M. Whitesides, The origins and the future of microfluidics, Nature 442 (2006) 368–373.
[2] X., Casadevall, i, Solvas,, A., deMello,, Droplet microfluidics: recent developments and future applications, Chem. Commun. 47 (2011) 1936–1942.
[3] P.S. Dittrich, A. Manz, Lab-on-a-chip: microfluidics in drug discovery, Nat. Rev. Drug Discov. 5 (2006) 210–218.
[4] A.J. deMello, Control and detection of chemical reactions in microfluidic systems, Nature 442 (2006) 394–402.
[5] A.B. Theberge, F. Courtois, Y. Schaerli, M. Fischlechner, C. Abell, F. Hollfelder, W. T.S. Huck, Microdroplets in microfluidics: an evolving platform for discoveries in chemistry and biology, Angew. Chem. Int. Ed. 49 (2010) 5846–5868.
[6] L. Yu, C. Ni, S.M. Grist, C. Bayly, K.C. Cheung, Alginate core-shell beads for simplified three-dimensional tumor spheroid culture and drug screening, Biomed. Microdev. 17 (2015) 33.
[7] A.B. Theberge, E. Mayot, A. El Harrak, F. Kleinschmidt, W.T.S. Huck, A.D. Griffiths, Microfluidic platform for combinatorial synthesis in picolitre droplets, Lab Chip 12 (2012) 1320–1326.
[8] H.N. Joensson, M. Uhlén, H.A. Svahn, Droplet size based separation by deterministic lateral displacement—separating droplets by cell-induced shrinking, Lab Chip 11 (2011) 1305–1310.
[9] A. Hochstetter, R. Vernekar, R.H. Austin, H. Becker, J.P. Beech, D.A. Fedosov, G. Gompper, S.-C. Kim, J.T. Smith, G. Stolovitzky, J.O. Tegenfeldt, B.H. Wunsch, K. K. Zeming, T. Krüger, D.W. Inglis, Deterministic lateral displacement: challenges and perspectives, ACS Nano 14 (2020) 10784–10795.
[10] H. Maenaka, M. Yamada, M. Yasuda, M. Seki, Continuous and size-dependent sorting of emulsion droplets using hydrodynamics in pinched microchannels, Langmuir 24 (2008) 4405–4410.
[11] Y. Chang, X. Chen, Y. Zhou, J. Wan, Deformation-based droplet separation in microfluidics, Ind. Eng. Chem. Res. 59 (2020) 3916–3921.
[12] M. Li, M. van Zee, K. Goda, D. Di Carlo, Size-based sorting of hydrogel droplets using inertial microfluidics, Lab Chip 18 (2018) 2575–2582.
[13] J.-C. Baret, O.J. Miller, V. Taly, M. Ryckelynck, A. El-Harrak, L. Frenz, C. Rick, M. L. Samuels, J.B. Hutchison, J.J. Agresti, D.R. Link, D.A. Weitz, A.D. Griffiths, Fluorescence-activated droplet sorting (FADS): efficient microfluidic cell sorting based on enzymatic activity, Lab Chip 9 (2009) 1850–1858.
[14] K. Zhao, D. Li, Direct current dielectrophoretic manipulation of the ionic liquid droplets in water, J. Chromatogr. A 1558 (2018) 96–106.
[15] J.H. Jung, K.H. Lee, K.S. Lee, B.H. Ha, Y.S. Oh, H.J. Sung, Optical separation of droplets on a microfluidic platform, Microfluid. Nanofluid. 16 (2014) 635–644.
[16] H. Cho, C.B. Chang, J.H. Jung, H.J. Sung, Lateral migration of a microdroplet under optical forces in a uniform flow, Phys. Fluids 26 (2014), 122001.
[17] A. Munaz, M.J.A. Shiddiky, N.-T. Nguyen, Recent advances and current challenges in magnetophoresis based micro magnetofluidics, Biomicrofluidics 12 (2018).
[18] Y. Jo, F. Shen, Y.K. Hahn, J.-H. Park, J.-K. Park, Magnetophoretic sorting of single cell-containing microdroplets, Micromachines 7 (2016) 56.
[19] S. Li, X. Ding, F. Guo, Y. Chen, M.I. Lapsley, S.C. Lin, L. Wang, J.P. McCoy, C. E. Cameron, T.J. Huang, An on-chip, multichannel droplet sorter using standing surface acoustic waves, Anal. Chem. 85 (2013) 5468–5474.
[20] I. Leibacher, P. Reichert, J. Dual, Microfluidic droplet handling by bulk acoustic wave (BAW) acoustophoresis, Lab Chip 15 (2015) 2896–2905.
[21] B. Selva, V. Miralles, I. Cantat, M.-C. Jullien, Thermocapillary actuation by optimized resistor pattern: bubbles and droplets displacing, switching and trapping, Lab Chip 10 (2010) 1835–1840.
[22] J. Park, J.H. Jung, G. Destgeer, H. Ahmed, K. Park, H.J. Sung, Acoustothermal tweezer for droplet sorting in a disposable microfluidic chip, Lab Chip 17 (2017) 1031–1040.
[23] Y. Qiao, X. Zhao, J. Zhu, R. Tu, L. Dong, L. Wang, Z. Dong, Q. Wang, W. Du, Fluorescence-activated droplet sorting of lipolytic microorganisms using a compact optical system, Lab Chip 18 (2018) 190–196.
[24] X. Niu, M. Zhang, S. Peng, W. Wen, P. Sheng, Real-time detection, control, and sorting of microfluidic droplets, Biomicrofluidics 1 (2007), 044101.
[25] K. Zhao, D. Li, Tunable droplet manipulation and characterization by ac-DEP, ACS Appl. Mater. Interfaces 10 (2018) 36572–36581.
[26] D. Vallejo, A. Nikoomanzar, B.M. Paegel, J.C. Chaput, Fluorescence-activated droplet sorting for single-cell directed evolution, ACS Synth. Biol. 8 (2019) 1430–1440.
[27] V. Skowronek, R.W. Rambach, L. Schmid, K. Haase, T. Franke, Particle Deflection in a Poly(dimethylsiloxane) Microchannel Using a Propagating Surface Acoustic Wave: Size and Frequency Dependence, Anal. Chem. 85 (2013) 9955–9959.
[28] V. Skowronek, R.W. Rambach, T. Franke, Surface acoustic wave controlled integrated band-pass filter, Microfluid. Nanofluid. 19 (2015) 335–341.
[29] D. Rabaud, P. Thibault, J.-P. Raven, O. Hugon, E. Lacot, P. Marmottant, Manipulation of confined bubbles in a thin microchannel: Drag and acoustic Bjerknes forces, Phys. Fluids 23 (2011), 042003.
[30] M. Saqib, O.B. Şahinoğlu, E.Y. Erdem, Alternating Droplet Formation by using Tapered Channel Geometry, Sci. Rep. 8 (2018) 1606.
[31] S. Zolotukhin, B.J. Byrne, E. Mason, I. Zolotukhin, M. Potter, K. Chesnut, C. Summerford, R.J. Samulski, N. Muzyczka, Recombinant adeno-associated virus purification using novel methods improves infectious titer and yield, Gene Ther. 6 (1999) 973–985.
[32] K.J. Andersen, H. Vik, H.P. Eikesdal, E.I. Christensen, Effects of Contrast Media on Renal Epithelial Cells in Culture, Acta Radiol. 36 (1995) 213–218.
[33] M. Goto, H. Yatsuda, T. Chiba, Power Flow Angles for Slanted Finger Surface Acoustic Wave Filters on Langasite Substrate, Jpn. J. Appl. Phys. 46 (2007) 4744–4748.
[34] S. Maramizonouz, M. Rahmati, A. Link, T. Franke, Y. Fu, Numerical and experimental studies of acoustic streaming effects on microparticles/droplets in microchannel flow, Int. J. Eng. Sci. 169 (2021), 103563.
[35] M.A.S. Pessôa, A.A.R. Neves, Acoustic scattering and forces on an arbitrarily sized fluid sphere by a general acoustic field, J. Sound Vib. 479 (2020), 115373.
[36] J. Park, J.H. Jung, K. Park, G. Destgeer, H. Ahmed, R. Ahmad, H.J. Sung, On-demand acoustic droplet splitting and steering in a disposable microfluidic chip, Lab Chip 18 (2018) 422–432.
[37] J. Park, G. Destgeer, H. Kim, Y. Cho, H.J. Sung, In-droplet microparticle washing and enrichment using surface acoustic wave-driven acoustic radiation force, Lab Chip 18 (2018) 2936–2945.
[38] J. Lee, K. Ha, K.K. Shung, A theoretical study of the feasibility of acoustical tweezers: Ray acoustics approach, J. Acoust. Soc. Am. 117 (2005) 3273–3280.
[39] J. Lee, K.K. Shung, Radiation forces exerted on arbitrarily located sphere by acoustic tweezer, J. Acoust. Soc. Am. 120 (2006) 1084–1094.
[40] A. Ashkin, Forces of a single-beam gradient laser trap on a dielectric sphere in the ray optics regime, Biophys. J. 61 (1992) 569–582.

[41] B. Issenmann, A. Nicolas, R. Wunenburger, S. Manneville, J.P. Delville, Deformation of acoustically transparent fluid interfaces by the acoustic radiation pressure, Europhys. Lett. 83 (2008) 34002.
[42] P. Augustsson, J.T. Karlsen, H.-W. Su, H. Bruus, J. Voldman, Iso-acoustic focusing of cells for size-insensitive acousto-mechanical phenotyping, Nat. Commun. 7 (2016) 11556.
[43] M. Sesen, T. Alan, A. Neild, Microfluidic on-demand droplet merging using surface acoustic waves, Lab Chip 14 (2014) 3325–3333.
[44] R.G.M. van der Sman, Drag force on spheres confined on the center line of rectangular microchannels, J. Colloid Interface Sci. 351 (2010) 43–49.
[45] Z. Yu, C.R. Boehm, J.M. Hibberd, C. Abell, J. Haseloff, S.J. Burgess, I. Reyna-Llorens, Droplet-based microfluidic analysis and screening of single plant cells, PLoS One 13 (2018) e0196810.
[46] K. Redenbaugh, S. Ruzin, J. Bartholomew, J.A. Bassham, Characterization and Separation of Plant Protoplasts Via Flow Cytometry and Cell Sorting, Z. Pflanzenphysiol. 107 (1982) 65–80.
[47] S. Ning, S. Liu, Y. Xiao, G. Zhang, W. Cui, M. Reed, A microfluidic chip with a serpentine channel enabling high-throughput cell separation using surface acoustic waves, Lab Chip 21 (2021) 4608–4617.
[48] L. Schmid, D.A. Weitz, T. Franke, Sorting drops and cells with acoustics: acoustic microfluidic fluorescence-activated cell sorter, Lab Chip 14 (2014) 3710–3718.
[49] D.R. Link, E. Grasland-Mongrain, A. Duri, F. Sarrazin, Z. Cheng, G. Cristobal, M. Marquez, D.A. Weitz, Electric Control of Droplets in Microfluidic Devices, Angew. Chem. Int. Ed. 45 (2006) 2556–2560.
[50] K. Zhang, Q. Liang, S. Ma, X. Mu, P. Hu, Y. Wang, G. Luo, On-chip manipulation of continuous picoliter-volume superparamagnetic droplets using a magnetic force, Lab Chip 9 (2009) 2992–2999.